NANO LETTERS

Letter

pubs.acs.org/NanoLett

Ultimate Bending Strength of Si Nanowires

G. Stan,*[,†] S. Krylyuk,[‡,§] A. V. Davydov,[‡] I. Levin,[†] and R. F. Cook[†]

[†]Ceramics Division and [‡]Metallurgy Division, National Institute of Standards and Technology, Gaithersburg, Maryland 20899, United States

[§]Institute for Research in Electronics and Applied Physics, University of Maryland, College Park, Maryland 20742, United States

ABSTRACT: Test platforms for the ideal strength of materials are provided by almost defect-free nanostructures (nanowires, nanotubes, nanoparticles, for example). In this work, the ultimate bending strengths of Si nanowires with radii in the 20−60 nm range were investigated by using a new bending protocol. Nanowires simply held by adhesion on flat substrates were bent through sequential atomic force microscopy manipulations. The bending states prior to failure were analyzed in great detail to measure the bending dynamics and the ultimate fracture strength of the investigated nanowires. An increase in the fracture strengths from 12 to 18 GPa was observed as the radius of nanowires was decreased from 60 to 20 nm. The large values of the fracture strength of these nanowires, although comparable with the ideal strength of Si, are explained in terms of the surface morphology of the nanowires.

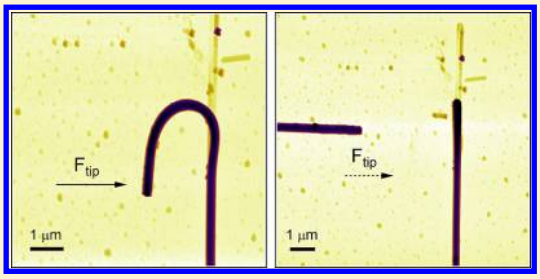

KEYWORDS: *Fracture strength, bending tests, Si nanowires, atomic force microscopy, nanomanipulation*

The functional reliability of small scale Si-based devices requires appropriate electrical,[1,2] optical,[3,4] mechanical,[5] piezoelectric,[6] and thermoelectric properties[7,8] of Si at micrometer and nanometer length scales. In considering the mechanical properties requirements, besides achieving the correct elastic response,[9] fracture strength is a limiting mechanical property that guides the selection and use of Si constituents in current electronic devices, microelectromechanical systems, and flexural and static structural applications.[10−12] The fracture strength of a brittle component is a composite property, combining both intrinsic (material resistance to fracture) and extrinsic (fabrication and processing induced stress-concentrating flaws) dependencies.[13] In the absence of flaws or defects, the intrinsic element determines the maximum stress that a material can sustain before fracture or structural transformation. This is referred to as the ideal or ultimate fracture strength, σ_f, and is roughly 10% of the elastic modulus E, $\sigma_f \approx E/10$.[14,15] For example, depending on the crystallographic direction, the ideal fracture strength of bulk Si is calculated to be between 15 and 25 GPa.[15,17] In practice, the fracture strength of Si at the microscale, for Si wafers and dies is usually 1 or 2 orders of magnitude less than these ideal limits (for recent reviews of the strength of Si refer to refs 13 and 16). This is attributed to various grown-in defects and processing-induced flaws that lead to stress-driven failure.

The relevance of the ideal fracture strength becomes more important to material property investigation at the nanoscale.[18−21] As the test specimen size is reduced to the nanometer scale, fracture strength is expected to attain greater fractions of the ideal limit due to the reduction of stress-concentrating flaw populations. Indeed, an increase of 20−40 times in the bending strength of Si beams was observed as the size was reduced from millimeters to nanometers.[22−24] Moreover, a nearly ideal strength has been sought in almost defect-free nanostructures (nanoparticles, nanotubes (NTs), nanowires (NWs), etc). In an attempt to observe the ultimate strength behavior of nanomaterials, the fracture strength of various one-dimensional nanostructures has been measured.[18,20,25−30] In particular, the fracture strength of Si NWs indicates a significant enhancement compared with measurements at millimeter and micrometer scales.[31−34]

Various tensile and bending protocols have been adapted from the macroscale to test the fracture strength of one-dimensional nanostructures. Tensile tests (stretching the specimen between two probes[20,25,29,34]) were performed inside a scanning electron microscope (SEM) or transmission electron microscope (TEM) to determine the ultimate strength values from the stress−strain response of measured NWs or NTs. Different bending tests in the form of cantilever configurations,[18,32,33] loops between two manipulators,[28] or three-point bending tests (stretching bridged filaments[26,27,31]) were used to observe the highest stress state sustained by a NW or NT just before failure. The bending of one-dimensional nanostructures was also investigated by using the stretching forces developed in the NWs' support during electron beam exposure in a TEM.[35,36] In the work here, by using atomic force microscopy (AFM) manipulation, Si NWs were bent into either hook or loop configurations. The NWs were simply held by adhesion on a flat Si substrate and the bending process was detailed after each incremental bending step through AFM imaging. A long segment of a NW was fixed by adhesion to the substrate and a hook or loop on a short end segment of the

Received: March 9, 2012
Revised: April 5, 2012
Published: April 11, 2012

   dx.doi.org/10.1021/nl300957a | *Nano Lett.* 2012, 12, 2599−2604

NW was formed by manipulation with the AFM probe; the adhesion between the NW and the substrate was strong enough to retain the imposed bending after the AFM probe was removed and subsequently used for imaging. Fracture strengths as great as 18 GPa were measured for the investigated Si NWs from the last observed bending states prior to fracture. The great advantage of this new protocol is that after each bending step, the NW can be imaged by AFM and the bending state can be analyzed with high spatial resolution; the bending states are observed statically after each displacement increment.

The Si NWs measured in this work were from the same batches of NWs for which the structure and elastic properties were investigated in previous works.[9,37] The NWs were synthesized by a Au-catalytic vapor−liquid−solid technique on Si(111) substrates at 500 °C in a mixture of SiH_4, N_2, and H_2 gases. From TEM electron diffraction and SEM electron backscatter diffraction the NWs were found to be single-crystals with their axes along the Si [11$\bar{2}$] direction. The elastic moduli of such Si NWs with radius in the 15−60 nm range were found to be approximately 160 GPa from contact-resonance AFM measurements.[9] The Si NWs were detached from their original substrate through a gentle sonication in isopropyl alcohol. A few drops of the resulting suspension were deposited on a clean Si(100) substrate. After the solution dried, straight NWs as long as 25 μm were observed on the substrate through simple inspections by SEM or AFM. The AFM topography scans around the NWs were performed with the microscope operated in intermittent contact mode and NW manipulation was performed by dragging the AFM probe along chosen directions in contact mode. The AFM used was a Bruker MultiMode with Controller V (Santa Barbara, CA) with PP-SEIH probes from Nanosensors (Neuchetal, Switzerland) (spring constant about 10 N/m).[38] Both topography and manipulation used conventional AFM operating modes. During AFM manipulation it was observed that the isopropyl alcohol promoted accumulation of contaminants on the Si surface and especially between the NWs and the substrate. These contaminants provided an enhanced adhesion between NWs and the substrate and a convenient pinning for NWs subjected to bending; the bending tests were performed on the free ends of a few long NWs. The displacement increments during bending manipulation were in the range 500−100 nm, larger in the initial bending stages and shorter in the final bending stages to allow a more detailed observation during the last stages prior to fracture. About 20 manipulation steps were found to provide a satisfactory observation of the bending process of an initially straight NW. After each manipulation step, the topography imaging to observe the imposed bending on a NW was made either at low spatial resolution (in the first bending stages) or at high spatial resolution (in the last bending stages). Each manipulation step took about 2 min and each topography imaging step took about 15 min; a single experiment took between 6 and 8 h.

Some of the manipulation steps performed during one of the bending tests are shown in Figure 1 for a Si NW of radius 57.5 nm; the NW was about 22 μm in length but only a third of the length was imaged sequentially after each bending step. Intermittent contact mode AFM was used to generate the images. Initially, the NW was straight (see Figure 1a) and a hook was produced at one end of the NW by dragging the AFM probe in contact with the substrate along directions perpendicular and parallel to the NW axis (Figure 1b−h to impose a force F_{tip} on the NW. Once a NW segment was displaced from its initial position, visible lines of residual

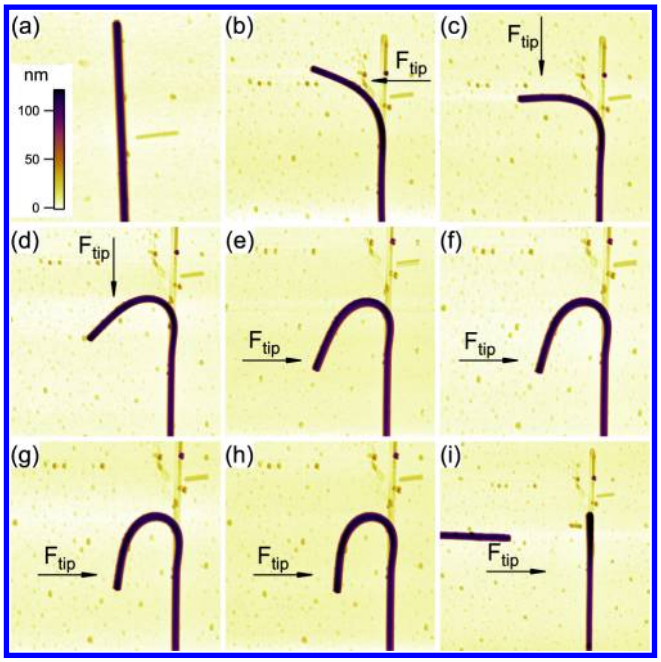

Figure 1. (a)−(h) Selected bending states before failure of a 57.5 nm radius Si NW as imaged by AFM. ((h) was the last imaged bending state before failure.) (i) Broken NW segments imaged after failure. The scan area is 7.5 μm × 7.5 μm in (a)−(h) and 10 μm × 10 μm in (i). The *z*-scale shown in (a) applies to all images.

contaminants were observed at prior NW locations. Also, as observable in Figure 1b, locations at which the tip was dragged on the surface were decorated with drops of contaminants from the NW−substrate contact. From the decorated trace made by the AFM probe and the position of the free end of the NW it could be discerned that the NW end had sprung back from the most bent state produced by the AFM probe at the greatest extent of probe motion. Such NW relaxations in moderate bending states were avoidable by performing the manipulation in small steps (of order of 100 nm) or starting to form the hook with a longer NW end segment such that the adhesion was greater on the displaced segment. In any case, the remaining long portion of the NW was held very well by adhesion to the substrate and was not observed to move during manipulation. After an initial hook was produced (Figure 1d), the radius of the hook was gradually reduced by pushing the short arm toward the long arm to close the formed hook (Figure 1e−h). The radius of the hook was decreased at each step until the most bent part of the NW (the upper part of the hook) broke and the built-up stress was released: The end of the long segment bounced back to its original alignment and the short segment flew to a nearby location (Figure 1i).

The bending states in the recorded AFM scans were analyzed to determine the bending moment and stress developed in NWs before fracture. Given that in the bending configurations developed the axial stress is negligible compared with the bending stress (only one end of the NW was fixed), the stress contribution at the point of fracture will be considered only from bending. Thus, for a linear elastic and isotropic rod in pure bending (in this case a NW of radius R_{NW}), the bending stress σ_b at the outer part of a bent NW is related to the local radius of curvature ρ by[39]

$$\sigma_b = R_{NW}E/\rho \quad (1)$$

where E is the elastic modulus of the NW.

dx.doi.org/10.1021/nl300957a | *Nano Lett.* 2012, 12, 2599−2604

The parameters used to calculate the bending stresses were the elastic moduli given above (as measured in ref 9), the NW radii measured directly from topographic cross sections, and the local radii of curvature from the in-plane deflection of the neutral axis of the NWs. To determine the local radius of curvature ρ, the x and y coordinates along the NW neutral axis were determined from the AFM scans[40] by using DataThief software[38,41] to locate the thickest part of the NW in each AFM image (i.e., to trace the middle line along the NW). The measured locations along the middle line were 100 nm apart. Once the x and y coordinates were determined, a parabolic fit at each location including six adjacent points (three on each side) was performed to find the radius of curvature given by

$$\rho = \left[1 + \left(\frac{dy}{dx}\right)^2\right]^{3/2} \left|\frac{d^2y}{dx^2}\right|^{-1} \quad (2)$$

with both derivatives calculated from the parabolic fit. Using the local radius of curvature, eq 1 was then used to calculate the bending stress profile along the NW.

A slightly different bending configuration can be generated by forming a closed loop during AFM manipulation (refer to Figure 2). In this case, long NW segments were brought next to each other and the radius of the loop formed between them was progressively reduced by pushing with the AFM probe from one side of the loop. The benefit of this configuration was a better anchoring of the manipulated NW by adhesion on the substrate; the bending moments at both ends of the loop were entirely canceled by the moments developed by the friction forces along the long NW segments. The last bending states before fracture in the loop configuration are detailed in Figure 2 for a Si NW of radius 39.2 nm. The NW was initially straight, along the oblique contamination line imaged by AFM in Figure 2a. By pushing along horizontal and vertical directions (see the trails of contamination spots in Figure 2a) the NW was bent into a closed loop configuration. Although some contaminants were deposited on the NW during manipulation, they did not appear to modify the strength of the NW; moreover, the bending region was not touched in the course of measurements. In the last bending stages, the NW sides were displaced in increments of about 100 nm. The last bending state was captured by chance during the imaging scan shown in Figure 2b when the NW broke and snapped while the AFM probe was scanning over it. After the snapping event, the AFM probe scanned upward over the flat substrate and the broken NW segment in its relaxed position instead of over the bent section of the NW (the scan direction in Figure 2b was from bottom to top); the violent snapping of the NW suggests brittle fracture as the failure mechanism. The scan was repeated in Figure 2c to confirm the NW fracture and observe the snapped segments; the lack of deformation in the snapped segments is also consistent with brittle fracture. The stress distribution in the last bending state was calculated from the local radius of curvature around the most bent part of the loop. This is shown in Figure 2d superimposed over the NW trace observed in Figure 2b. The ultimate bending stress sustained by this NW in the most bent region was determined to be 18.5 GPa, with a corresponding strain of 11.5%.

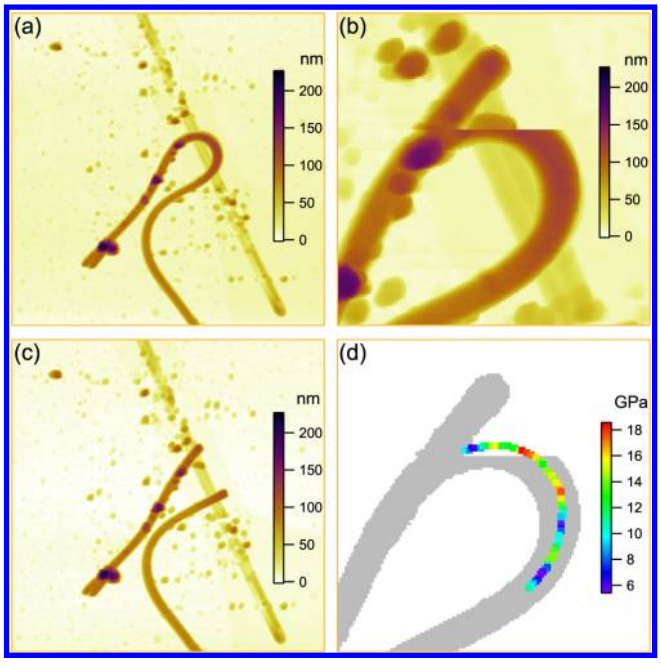

Figure 2. Si NW bent into a loop configuration. (a) A 7.5 μm × 7.5 μm scan captured the working field; the horizontal and vertical lines of contamination spots marked the traces along which the tip was dragged into contact with the substrate to form the loop. (b) An enlarged 2 μm × 2 μm area details the last bending stage. During the scanning (horizontally from bottom to top) over the most bent part of the loop, the NW broke under the scanning probe and snapped laterally. (c) After the scan in (b), the broken NW is shown in a 7.5 μm × 7.5 μm scan. (d) The bending stress distribution along the most bent part of the loop was calculated for the last bending state shown in (b).

The results of the bending measurements on Si NWs are shown in Figure 3 as the maximum stress in the last observed bending state plotted versus the NW radius. For the range of NW radii investigated in these measurements, an increase in the fracture strength of Si NWs was observed from about 12 GPa to about 18 GPa as the NW radius decreased from 60 to 20 nm. In contrast to this observation, no clear radius dependence was found within the same NW radius range for the radial elastic modulus of these Si NWs.[9] The maximum fracture strength values measured here are comparable with the calculated ideal tensile strength of Si along the ⟨110⟩ direction, 17.0 GPa[17]

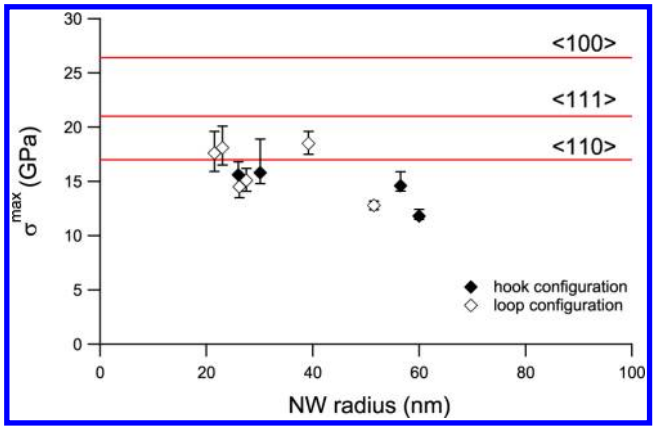

Figure 3. Maximum bending stress as a function of NW radius. The filled and open symbols are the maximum stresses measured in the hook and loop bending configurations, respectively. The lines indicate the ideal tensile strengths found in simulations for the principal crystallographic direction of Si.[17]

dx.doi.org/10.1021/nl300957a | Nano Lett. 2012, 12, 2599−2604

(refer to continuous lines in Figure 3). The uncertainties in Figure 3 were calculated by considering a 20 nm uncertainty in the fitting values for the radii of curvature; an additional 50 nm was considered as an upper bound to the uncertainty for the radius of curvature in each hook configuration (in some cases the true last bending state was inferred from the position of some contaminants).

Previously, by measuring the vertical deflection of Si[111] NWs connected to their native Si(111) substrate, fracture strengths in the range 7−18 GPa were measured for the NW−substrate junctions.[32] The variation observed in ref 32, i.e., reduced strength for longer NWs, was rationalized in terms of neglecting the tensile stress contribution to the loading for the longest tested NWs rather than as a radius dependence for the fracture strength of Si NWs with radii in the 50−100 nm range. Radius dependencies of the fracture strengths for Si NWs have been observed, although at smaller fracture strength values: The fracture strength increased from 5 to 12 GPa as the NW radius decreased from 60 to 15 nm in tensile tests on Si[111] NWs[34] and from 0.03 to 4 GPa as the NW radius decreased from 200 to 50 nm in cantilever-bending tests on Si[111] NWs.[33]

Details of the internal microstructure of the Si NWs measured in this work were provided by electron diffraction and TEM investigation (refer to Figure 4). Both electron

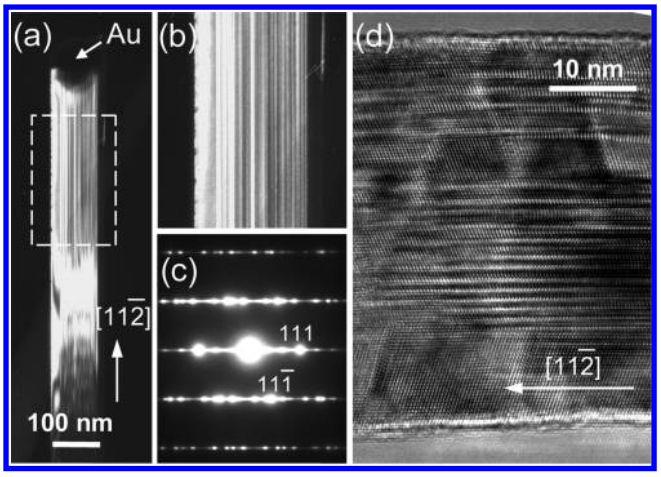

Figure 4. (a) Dark-field TEM image of a typical Si NW (radius 50 nm) recorded using 111-type reflection strongly excited near the ⟨110⟩ zone axis orientation. (b) Magnified view of the image part outlined in (a). A high density of planar defects (i.e., stacking faults, twin boundaries) parallel to the NW axis is observed. (c) Selected area ⟨110⟩ zone axis electron diffraction pattern from the same NW. Pronounced diffuse streaking perpendicular to the defect planes is observed. Extra spots along the [111] direction are attributed to double diffraction on twinned parts of the NW. (d) High-resolution TEM image of a typical Si NW (radius 23 nm) reveals a high-density of planar defects similar to that seen for the NWs having larger diameters. The [11$\bar{2}$] NW axis in this image is horizontal.

diffraction patterns and high-resolution TEM images on either thick (about 50 nm radius) or thin (about 23 nm radius) NWs showed that the NWs were single-crystalline Si structures oriented along the crystallographic [11$\bar{2}$] direction. As can be seen in Figure 4a,b,d, (111) planar defects (i.e., stacking faults, twin boundaries) along the axis of the NWs were commonly observed in dark-field and high-resolution TEM images. Also, the presence of the planar defects can be inferred from the enhanced diffused streaking perpendicular to the (111) planes observed in electron diffraction patterns (Figure 4c). From the analysis of dark-field and high-resolution TEM images, similar densities of these planar defects were estimated for both thick and thin Si NWs. High-resolution TEM images revealed surface irregularities and oxide layers confined within a surface region of about 2 nm in thickness.

Some characteristic aspects of the fracture dynamics of the investigated Si NWs were inferred from the postfracture analysis of their broken ends. In all the cases, the fractures appeared to be brittle (without plastic deformations); no tapering was observed at the broken ends as imaged by AFM before or after fracture, and the broken NW segments were found to relax violently into stress-free states. In Figure 5a−d,

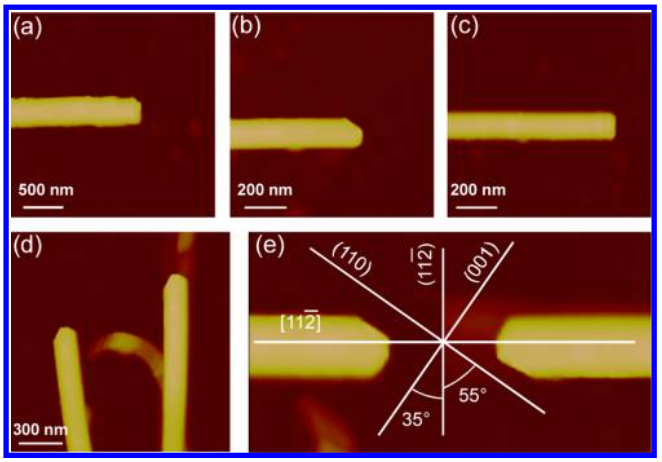

Figure 5. (a)−(d) Typical broken ends observed in the bending fracture experiments in this work. (e) The broken ends shown in (d) were realigned along the NW axis. Crystallographic directions and planes are shown here with respect to the [11$\bar{2}$] direction of the cubic crystal system.

typical broken ends observed in these bending fractures were detailed in postfracture AFM scans. In Figure 5d, the bending state before fracture is indicated by the contamination trace between the two broken ends. The relaxation of the two broken NW segments into straight positions demonstrates an elastic bending behavior prior to the brittle fracture. As can be seen in Figure 5a−d, the fracture either propagated normal to the NW axis all the way across the NW or propagated on cleavage planes within the regions of the highest tension and compression. These cleavage planes are analyzed in Figure 5e, in which the images of the broken ends from the fracture shown in Figure 5e are realigned along the axis of the NW. Considering the crystallographic orientation of the NWs, the fracture facets of (110), (11$\bar{2}$), and (001) are revealed.

The scale of the defects controlling the fracture strength of the Si NWs can be estimated by $RE/(\sigma^{max})^2$, where R is the fracture resistance of the NW. Using the strength values in Figure 3, E = 160 GPa, and R = 3 J m^{-2} [13] (an average value for bulk Si) gives defects in the range 1.5−3.3 nm, comparable in size to the stacking fault defects and oxidized surface layers shown in the NW images of Figure 4. The increase in strength with decreasing radius observed in Figure 3 suggests that larger defects were less common in the smaller NWs. This observation indicates that the stacking faults in the volume of the NWs were not the strength-limiting defects because the scale of the stacking faults did not vary with NW radius and, if strength-controlling, they would have led to an invariant strength. Instead, as the NW radius decreased, the surface area

dx.doi.org/10.1021/nl300957a | Nano Lett. 2012, 12, 2599−2604

of the NW decreased and the probability of a large surface defect decreased, leading to an increase in strength. The form of the surface defects is probably a nanoscale crack, perhaps at the root of a nanoscale notch associated with the surface roughness. Comparison of the strengths of many Si structures fabricated by many methods shows a strong correlation between the measured strength and the stressed area; smaller areas exhibit larger strengths.[16,22] The tensile stressed area here of approximately 0.1 μm^2 and strengths in excess of 10 GPa are entirely consistent with these broader observations, further supporting the contention that the strengths are surface defect controlled.

The fracture resistance of Si is anisotropic, with {111} as the preferred cleavage planes, followed by {110}, {112}, and {100}.[13] Observations of the broken ends of the Si NWs suggests that the direction of the tensile stress along the $[11\bar{2}]$ direction was the dominant influence in determining the fracture path, leading to single planar $(11\bar{2})$ fracture surfaces as shown in Figure 5a,c. In some cases, (110) and (001) fracture surface elements were formed along with a $(11\bar{2})$ surface element, leading to a multifaceted surface, as shown in Figure 5b,d. The vertical and diagonal lines in Figure 5e indicate the traces of the $(11\bar{2})$, (110), and (001) planes in the $(1\bar{1}0)$ image plane. Fracture surfaces such as those shown in Figure 5e were probably formed by crack bifurcation after extension of an initial crack. When high strength components fracture, large crack velocities occur and instabilities in the propagating crack tip stress field develop such that the maximum crack driving force occurs at an angle to the crack plane, leading to crack deflection and bifurcation from the initial plane.[13,16,42] In this case the initial crack propagation was on the $(11\bar{2})$ plane, followed by crack bifurcation onto the (001) and (110) planes. The large amounts of stored elastic energy generated during high strength fracture are often released as kinetic energy of fragments formed by the bifurcation process. Hence the missing triangular elements of material bound by the (001), (110), and (111) planes in Figure 5e were probably rapidly ejected from the NW and do not appear in the image. Similar fracture surfaces with missing triangular fragments were formed on larger samples, in which fracture initiated on the (110) plane perpendicular to the tensile axis and bifurcated onto the $(\bar{1}1\bar{1})$ and $(11\bar{1})$ planes;[16] in this case the crack bifurcated onto planes of smaller fracture resistance. It is extremely likely that the fracture paths of the NWs were strongly influenced by the stacking faults, leading to fracture on planes with fracture resistance greater than the preferred {111} cleavage.

Several previous studies have also observed brittle fracture of Si NWs.[32−34] The diameters of the Si NWs exhibiting brittle fracture were usually larger than 50 nm, although brittle fracture was confirmed for Si NWs as thin as 15 nm in diameter.[34] There are also reports of ductile fracture of Si NWs with plastic deformation preceding failure for Si NWs observed in the TEM.[35,36,43,44] The ductile fractures were mostly observed for thin Si NWs with diameters in the 10−50 nm range and a ductile-to-brittle transition diameter about 60 nm was found for Si[110] NWs.[35] A possible effect of the TEM electron beam on the material structure in the exposed regions of the NWs[45,46] is to increase dislocation activity within these regions leading to ductility prior to failure. It has been shown[45] that the plastic deformability of brittle nanostructures investigated by TEM arises through induced local amorphization under exposure to the high-energy radiation of the electron beam. One advantage of the technique proposed in the present work is that it eliminates any intrusive contaminations or structural perturbations in the fracture region.

In this work, a new method has been demonstrated for observing large bending stress states of $[11\bar{2}]$ Si NWs by using a sequential AFM manipulation-scanning protocol. Adhesion between the NWs and a substrate provided strong-enough forces to maintain the NWs in the imposed bending states. The benefit of the method is that it does not require special grips at the ends of the NW tested and allows a postobservation of the bending states. In various bending configurations (hook and loop), it was possible to observe large bending stress states of Si NWs as their radius of curvature was progressively reduced. A slight increase in the fracture strength of Si NWs from 12 to 18 GPa as their radius decreased from 60 to 20 nm was observed in these measurements. Although comparable with the ideal limit of the fracture strength of Si, the observed large values of the fracture strength of the investigated NWs were explained in terms of internal microstructure and surface morphology of the NWs. The radius dependence of the fracture strength can be rationalized as a surface effect. As the NW radius is reduced, the coaxial near-surface region around the NW decreases in size and limits the amounts of surface stress-concentrating flaw populations (in terms of surface roughness and oxide presence).

AUTHOR INFORMATION

Corresponding Author

*Electronic mail: gheorghe.stan@nist.gov.

Notes

The authors declare no competing financial interest.

REFERENCES

(1) Cui, Y; Duan, X.; Hu, J.; Lieber, C. M. *J. Phys. Chem. B* **2000**, *104* (22), 5213−5216.

(2) Duan, X.; Niu, C; Sahi, V; Chen, J.; Wallace Parce, J.; Empedocles, S.; Goldman, J. L. *Nature* **2003**, *425* (6955), 274−278.

(3) Huang, Y.; Duan, X.; Lieber, C. M. *Small* **2005**, *1* (1), 142−147.

(4) Tian, B.; Zheng, X.; Kempa, T. J.; Fang, Y.; Yu, N.; Yu, G.; Huang, J.; Lieber, C. M. *Nature* **2007**, *449* (7164), 885−890.

(5) Feng, X. L.; He, R.; Yang, P.; Roukes, M. L. *Nano Lett.* **2007**, *7* (7), 1953−1959.

(6) He, R.; Yang, P. *Nat. Nanotechnol* **2006**, *1* (1), 42−46.

(7) Hochbaum, A. I.; Chen, R.; Delgado, R. D.; Liang, W.; Garnett, E. C.; Najarian, M.; Majumdar, A; Yang, P. *Nature* **2008**, *451* (7175), 163−168.

(8) Boukai, A. I.; Bunimovich, Y.; Tahir-Kheli, J.; Yu, J.-K.; Goddard, W. A., III; Heath, J. R. *Nature* **2008**, *451* (7175), 168−171.

(9) Stan, G.; Krylyuk, S.; Davydov, A. V.; Cook, R. F. *Nano Lett.* **2010**, *10* (6), 2031−2037.

(10) Jadaan, O. M.; Nemeth, N. N.; Bagdahn, J.; Sharpe, W. N., Jr. *J. Mater. Sci.* **2003**, *38* (20), 4087−4113.

(11) Hartzell, A. L.; da Silva, M. G.; Shea, H. R. *MEMS Reliability*; Springer: New York, 2011.

(12) Khang, D.-Y.; Jiang, H; Huang, Y; Rogers, J. A. *Science* **2006**, *311*, 208−212.

(13) Cook, R, F. *J. Mater. Sci.* **2006**, *41* (3), 841−872.

(14) Felbeck, D. K.; Atkins, A. G. *Strength and fracture of engineering solids*; Prentice-Hall: Englewood Cliffs, NJ, 1984.

(15) Kelly, A.; Macmillan, N. H. *Strong solids*, 3rd ed.; Oxford University Press: New York, 1986.

(16) Gaither, M. S.; DelRio, F. W.; Gates, R. S.; Cook, R. F. *J. Mater. Res.* **2011**, *26* (20), 2575−2589.

(17) Dubois, S. M.-M.; Rignanese, G.-M.; Pardoen, T.; Charlier, J.-C. *Phys. Rev. B* **2006**, *74* (23), 235203−7.

(18) Wong, S. S.; Sheehan, P. E.; Lieber, C. M. *Science* **1997**, *277* (5334), 1971−1975.
(19) Lourie, O.; Cox, D. M.; Wagner, H. D. *Phys. Rev. Lett.* **1998**, *81* (8), 1638−1641.
(20) Kaplan-Ashiri, I.; Cohen, S. R.; Gartsman, K.; Ivanovskaya, V.; Heine, T.; Seifert, G.; Wiesel, I.; Wagner, H. D.; Tenne, R. *Proc. Natl. Acad. Sci. U. S. A.* **2006**, *103* (3), 523−528.
(21) Zhu, T.; Li, J.; Ogata, S.; Yip, S. *MRS Bull.* **2009**, *34* (3), 167−172.
(22) Namazu, T.; Isono, Y.; Tanaka, T. *J. Microelectromech. Syst.* **2000**, *9* (4), 450−459.
(23) Li, X.; Bhushan, B *Surf. Coat. Technol.* **2003**, *163−164*, 521−526.
(24) Li, X.; Bhushan, B.; Takashima, K.; Baek, C. W.; Kim, Y. K. *Ultramicroscopy* **2003**, *97* (1−4), 481.
(25) Yu, M. F.; Lourie, O.; Dyer, M. J.; Moloni, K.; Kelly, T. F.; Ruoff, R. S. *Science* **2000**, *287* (5453), 637−640.
(26) Wu, B.; Heidelberg, A.; Boland, J. J. *Nat. Mater.* **2005**, *4* (7), 525−529.
(27) Ngo, L. T.; Almecija, D.; Sader, J. E.; Daly, B.; Petkov, N.; Holmes, J. D.; Erts, D.; Boland, J. J. *Nano Lett.* **2006**, *6* (12), 2964−2968.
(28) Smith, D. A.; Holmberg, V. C.; Korgel, B. A. *ACS Nano* **2010**, *4* (4), 2356−2362.
(29) Brambilla, G.; Payne, D. N. *Nano Lett.* **2009**, *9* (2), 831−835.
(30) Richter, G.; Hillerich, K.; Gianola, D. S.; Mönig, R.; Kraft, O.; Volkert, C. A. *Nano Lett.* **2009**, *9* (8), 3048−3052.
(31) Tabib-Azar, M.; Nassirou, M.; Wang, R.; Sharma, S.; Kamins, T. I.; Islam, M. S.; Williams, R. S. *Appl. Phys. Lett.* **2005**, *87* (11), 113102−3.
(32) Hoffmann, S.; Utke, I.; Moser, B.; Michler, J.; Christiansen, S. H.; Schmidt, V.; Senz, S.; Werner, P.; Gösele, U.; Ballif, C. *Nano Lett.* **2006**, *6* (4), 622−625.
(33) Gordon, M. J.; Baron, T.; Dhalluin, F.; Gentile, P.; Ferret, P. *Nano Lett.* **2009**, *9* (2), 525−529.
(34) Zhu, Y.; Xu, F.; Qin, Q.; Fung, W. Y.; Lu, W. *Nano Lett.* **2009**, *9* (11), 3934−3939.
(35) Han, X.; Zheng, K.; Zhang, Y.; Zhang, X.; Zhang, Z.; Wang, Z. L. *Adv. Mater.* **2007**, *19* (16), 2112−2118.
(36) Zheng, K.; Han, X.; Wang, L.; Zhang, Y.; Yue, Y.; Qin, Y.; Zhang, X.; Zhang, Z. *Nano Lett.* **2009**, *9* (6), 2471−2476.
(37) Krylyuk, S.; Davydov, A. V.; Levin, I.; Motayed, A.; Vaudin, M. D. *Appl. Phys. Lett.* **2009**, *94* (6), 063113−3.
(38) Any mention of commercial products in this article is for information only; it does not imply recommendation or endorsement by the NIST.
(39) Landau, L. D.; Lifshitz, E. M. *Theory of elasticity*, 3rd ed.; Pergamon Press: New York, 1986.
(40) Strus, M. C.; Lahiji, R. R.; Ares, P.; Lopez, V.; Raman, A.; Reifenberger, R. *Nanotechnology* **2009**, *20* (38), 385709−8.
(41) Tummers, B. *Datathief III*, http://datathief.org/ Datathief is a program used to reverse engineering data points from a graph.
(42) Lawn, B. R. *Fracture of brittle solids*; Cambridge University Press: Cambridge, U.K., 1993.
(43) Wang, L; Zheng, K; Zhang, Z.; Han, X. *Nano Lett.* **2011**, *11* (6), 2382−2385.
(44) Tang, D. M.; Ren, C. L.; Wang, M. S.; Wei, X.; Kawamoto, N.; Liu, C.; Bando, Y.; Mitmoe, M.; Fukata, N.; Golberg, D. *Nano Lett.* **2012**, DOI: 10.1021/nl204282y.
(45) Zheng, K.; Wang, C.; Cheng, Y. Q.; Yue, Y.; Han, X.; Zhang, Z.; Shan, Z.; Mao, S. X.; Ye, M.; Yin, Y.; Ma, E. *Nat. Commun.* **2010**, *1*, 24.
(46) Zang, J.; Bao, L.; Webb, R. A.; Li, X. *Nano Lett.* **2011**, *11*, 4885−4889.